



Fabrication of $\text{TiO}_2/\text{RGO}/\text{Cu}_2\text{O}$ heterostructure for photoelectrochemical hydrogen production

Weiqliang Fan, Xiaoqiang Yu, Hua-Chang Lu, Hongye Bai, Chao Zhang, Weidong Shi*

School of Chemistry and Chemical Engineering, Jiangsu University, Zhenjiang 212013, PR China

ARTICLE INFO

Article history:

Received 4 June 2015

Received in revised form 17 July 2015

Accepted 19 July 2015

Available online 26 July 2015

Keywords:

Photoelectrochemistry

Hydrogen production

Heterostructure

Reduced graphene oxide

Cu_2O

ABSTRACT

Novel heterostructure built from titanium dioxide (TiO_2), reduced graphene oxide (RGO) and cuprous oxide (Cu_2O) has been successfully designed and prepared for photoelectrochemical hydrogen production. The stepwise introduction of three materials on conductive glass substrate has been realized through hydrothermal and chemical solution deposition methods, respectively. The morphology of Cu_2O regularly altered with increasing the amount of Cu_2O . The photoelectrochemical performance of heterostructure was systematically investigated, and the synergistic effect of TiO_2 , RGO and Cu_2O was conducive to improving the absorption spectrum range and electron/hole separation, which resulted in the enhancement of photocurrent intensity and incident photon-to-photocurrent efficiency. Electrochemical impedance spectroscopy (EIS) further confirmed that $\text{TiO}_2/\text{RGO}/\text{Cu}_2\text{O}$ heterostructure possessed the lowest charge-transfer resistance, revealing that heterostructure could significantly accelerate the electron mobility compared with bare TiO_2 . More importantly, the hydrogen production rate of $\text{TiO}_2/\text{RGO}/\text{Cu}_2\text{O}$ heterostructure was up to $631.6 \mu\text{mol/h m}^2$ (radiation intensity: 47 mW/cm^2) which is almost three times than that of bare TiO_2 .

© 2015 Published by Elsevier B.V.

1. Introduction

In recent decades, the primary energy source is met by fossil fuels, which accounts for approximately 85% of all energy. However, excessive consumption of this non-renewable resource has led to massive emissions of carbon dioxide (CO_2), resulting in world greenhouse effect. Therefore, it becomes a challenge for people to exploit alternative green energy sources [1–3]. As a kind of inexhaustible green energy, solar energy has attracted widely attention for many years, and photoelectrochemical cells is an effective device to realize the conversion of solar light to hydrogen energy by water splitting. Photoelectrode especially composed of semiconductors plays the most important role in light absorption, electron–hole pair's generation and charge transfer of photoelectrochemical cells. Taking account of synergistic effect between different semiconductors, fabrication of heterostructure were in-depth investigated, because of its ability to obviously enhance photoelectrochemical performance of photoelectrodes [4,5].

Among various semiconductors, titanium dioxide (TiO_2) is a popular matrix in the field of photoelectrochemical hydrogen

production, due to its favorable properties, such as superior chemical stability, strong oxidizing activity, non-toxicity and photocorrosion resistance [6,7]. Unfortunately, the solar energy utilization efficiency of bare TiO_2 is limited, since wide bandgap (3.2 eV) causes the ineffective absorption of visible light and insufficient photogenerated electrons [8]. Moreover, the recombination of electron–hole pairs inside TiO_2 matrix is another restriction. In order to overcome the shortcomings of bare TiO_2 , one of effective strategies is to sensitize TiO_2 with narrow bandgap semiconductors for constructing heterostructure [9]. Cuprous oxide (Cu_2O) has been applied as an attractive photoelectrode material for hydrogen production, because Cu_2O is a p-type semiconductor with narrow bandgap (1.9–2.2 eV) of which the conduction band and valence band are close to the reduction and oxidation potential for water splitting [10–13]. As previous reports [14,15], wide bandgap semiconductor (such as TiO_2 and ZnO) modified with Cu_2O nanoparticles can significantly expand their absorption spectra range. However, the low interfacial area between different semiconductors directly influenced the separation efficiency of electrons and holes, so interfacial optimization of heterogeneous becomes a feasible way to further improving photoelectrochemical conversion efficiency.

Graphene with two-dimensional structure has been used as excellent charge transfer medium, due to its high conductivity, excellent conductivity, high mobility of charge carriers and

* Corresponding author.

E-mail address: swd1978@ujs.edu.cn (W. Shi).

light transmission [16,17]. It has been found that graphene shows excellent link function for different semiconductor nanoparticles, which facilitates their interfacial contact and photogenerated electron–hole transmission [18,19]. However, it is difficult to make graphene well disperse in water due to its surface hydrophobicity, so graphene have seldom been used in preparation of composite material especially in aqueous solution. Graphene oxide (GO) with rich hydrophilic groups has raised concern in synthesis of composited materials for its high dispersion in water, which offers an opportunity for fabrication of heterostructure based on GO [20,21]. Though conductivity of GO is relatively bad, the reduced graphene oxide (RGO) as intermediate state between graphene and GO has the similar properties with graphene, which endows RGO with wide application [22]. Inspired by the above, introduction of both Cu_2O and RGO into photoelectrode might break the limitation of TiO_2 for photoelectrochemical water splitting. As far as we know, there are no corresponding reports about photoelectrode built from TiO_2 , Cu_2O and RGO up to now, so it will be a challenge to design and fabricate this kind of heterostructure photoelectrodes.

In this work, we successfully prepared novel heterostructure built from TiO_2 nanowires (NWs) arrays, RGO nanosheets (NSs) and Cu_2O , as an efficient photoelectrode for photoelectrochemical water splitting. TiO_2 NWs were synthesized by hydrothermal method on fluorine doped tin oxide conductive glass (FTO) substrates firstly, then RGO NSs were coated on the top of TiO_2 NWs through spin coating method, and Cu_2O were successfully loaded on the surface of RGO NSs via chemical solution deposition finally. Linear sweep voltammograms, electrochemical impedance spectroscopy (EIS) and incident photon-to-photocurrent efficiency (IPCE) were characterized in-depth to investigate the influence of Cu_2O and RGO on the photoelectrode. Taking account of the enhanced photoelectrochemical performance, the hydrogen production over $\text{TiO}_2/\text{RGO}/\text{Cu}_2\text{O}$ heterostructure was further measured by three electrode system.

2. Experimental

2.1. Synthesis of TiO_2 nanowires (NWs) on FTO glass

The TiO_2 NWs were synthesized by hydrothermal method on FTO substrate ($1\text{ cm} \times 1.5\text{ cm}$). Solution of deionized water (15 mL), HCl (15 mL) and tetrabutyl titanate (0.7 mL) was transferred into a Teflon-lined stainless steel autoclave (25 mL). The FTO substrates were pre-cleaned by water, acetone and chloroform, respectively. A piece of pre-cleaned FTO substrates was place into the Teflon-lined stainless steel autoclave and heated at 180°C for 6 h. The obtained samples were washed by deionized water several times, then it was put in a Muffle furnace and annealed at 450°C for 2 h [7,23,24].

2.2. Synthesis of TiO_2 NWs coated by RGO nanosheets (NSs)

GO has been synthesized through modified Hummer's and Offenman's method previously [25]. 0.1 g GO was dispersed in 5 mL deionized water by sonication, 2 drops of the GO solution were added on surface of TiO_2 NWs, and GO homogenous films were formed by spin coating method. The sample was transferred into a tube furnace in N_2 at 400°C for 2 h, which partially reduced GO and improved adhesion between the RGO and TiO_2 [26]. Finally, the obtained samples were soaked in deionized water under UV light illumination for 2 h to further reduce GO to RGO [27,28].

2.3. Synthesis of TiO_2 NWs/RGO NSs/ Cu_2O

Four solutions of 50 mL (0.1 M CuSO_4 and 0.1 M $\text{Na}_2\text{S}_2\text{O}_3$), 50 mL H_2O , 50 mL (0.1 M NaOH) and 50 mL H_2O were prepared in four beakers, respectively. The FTO/ TiO_2 /RGO samples were

immersed into the four solutions for approximately 10 s one after the other, and the completion of immersing above four solutions was recorded as a circle. The obtained samples were synthesized by 30, 60 and 90 cycled times, respectively. Finally, the samples were dried in the air.

2.4. Characterization

Scanning electron microscopy (SEM) was measured through S-4800 II field-emission scanning electron microanalyzer with an accelerating voltage (15 kV). Transmission electron microscopy (TEM) and high-resolution TEM (HR-TEM) were characterized on JEM-2100 (HR) microscopes connected with field-emission gun at acceleration voltage (200 kV). Electrochemical impedance spectra (EIS) analysis was measured in a three electrode configuration by CHI660 B electrochemical analyzer (CH Instruments). X-ray photoelectron spectroscopy (XPS, VG, Physical Electrons Quantum 2000 Scanning Esca Microprob, Al K α radiation) was used to measure the elements of samples. Raman spectra were collected on a Jobin-Yvon HR-800 spectrometer with a 488 nm Ar^+ ion laser at room temperature.

Photoelectrochemical measurements were investigated in a three-electrode cell, using 0.5 M Na_2SO_4 electrolyte, and the irradiation area is 1 cm^2 under 150 W xenon lamp (radiation intensity: $47\text{ mW}/\text{cm}^2$). The potential and other parameters were measured through an electrochemical workstation (CH Instruments, CHI 852C). Incident photon to current conversion efficiency (IPCE) was measured by external quantum efficiency measurement system (Newport/Oriel, QE-PV-SI) connected with electrochemical workstation. Photoelectrochemical water splitting experiments were monitored at 0.6 V vs Ag/AgCl under full-spectrum illumination, where hydrogen generated from Pt plate using gas chromatography (GC-7800, Beijing ZhongKe Technology Co.).

3. Results and discussion

The proposed synthesis process is shown in Fig. 1. The heterostructure photoelectrode built from TiO_2 NWs, RGO NSs and Cu_2O has been successfully designed and synthesized, and the morphology of Cu_2O can be easily adjusted to nanoparticles (NPs), nanoneedles (NNs) or nanosheets clusters (NSc) by varying the number of cycles.

The obtained samples were first characterized by FE-SEM. As shown in Fig. 2a, the uniform TiO_2 NWs with about 40–60 nm diameters vertically grew on surface of FTO substrate, which indicates that the morphology of TiO_2 NWs has been well controlled by hydrothermal method. After spin coated process and subsequent heat-treatment in N_2 atmosphere, the RGO NSs with folds were totally covered on the TiO_2 NWs (Fig. 2b). $\text{TiO}_2/\text{Cu}_2\text{O}$ without RGO sample is shown in Fig. 2c, Cu_2O with different morphology such as NPs and NNs (length is $\sim 1.5\text{ }\mu\text{m}$) has been built up on surface of TiO_2 NWs, and the same phenomenon has also been observed in the $\text{TiO}_2/\text{RGO}/\text{Cu}_2\text{O}$ samples (Fig. 2d–g), which reveals that the introduction of RGO would not influence the final morphology Cu_2O significantly. It can be also observed that TiO_2 NWs, RGO NSs and Cu_2O has been connected with each other from the damaged position of RGO NSs (Fig. 2d). According to the SEM images, the growth mechanism for different morphology of Cu_2O can be deduced as follow: during the deposition process, Cu_2O would first appeared as small crystal nucleus on the surface of RGO, then the crystal nucleus gradually grew and formed NPs and NNs with increasing the cycled times. The NNs numbers further increased, which finally resulted in the formation of NSc. Therefore, this SEM results confirmed that the morphology of NSc can be artificially controlled by altering cycle times. The images of cross-sectional sample (cycle = 60) gave

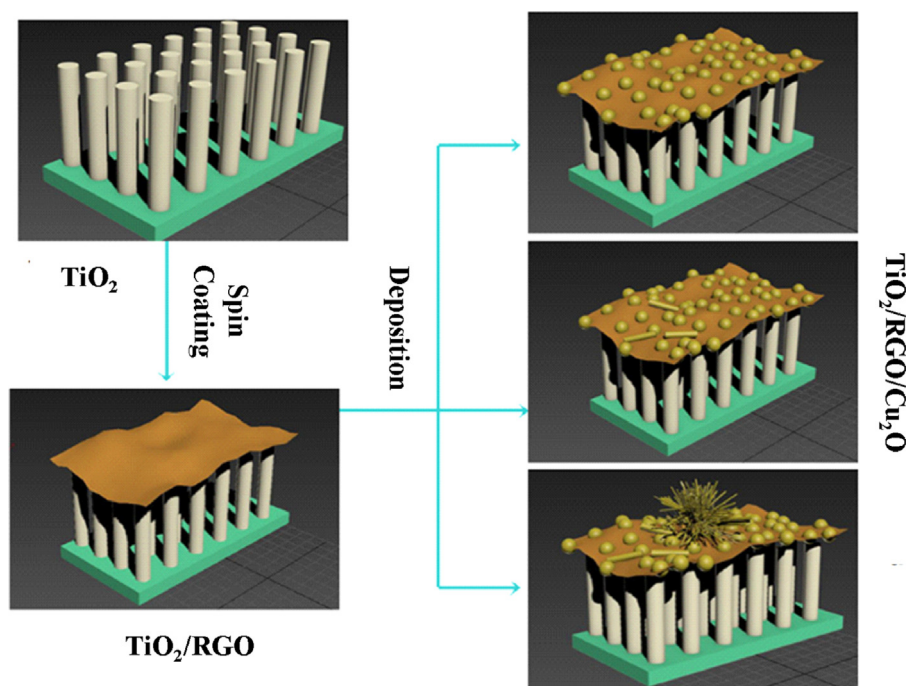


Fig. 1. Synthesis process of heterostructure photoelectrodes.

a proof that the morphology of TiO₂ nanowires has well remained after loading RGO and Cu₂O, as shown Fig. 2h.

XRD patterns (Fig. 3) were performed to investigate the crystal phase structure of photoelectrode, and the samples were measured in the form of powders which have been stripped from FTO substrate. The diffraction peaks of TiO₂ (PDF: 78-1510) can be observed in TiO₂, TiO₂/RGO and TiO₂/RGO/Cu₂O samples, which well confirmed the formation of TiO₂. While the successful introduction of Cu₂O in TiO₂/RGO/Cu₂O photoelectrodes can be identified by the two new peaks at the 2θ of 36° and 42° that ascribed to (1 1 1) and (2 0 0) of Cu₂O (PDF: 77-0199). However, the RGO was not distinguished by XRD patterns, caused by the low content and crystallinity of RGO film on the FTO. In order to illustrate the existence of RGO, Raman spectroscopy of TiO₂/RGO/Cu₂O photoelectrode was also analyzed in detail (Fig. 4), because RGO, TiO₂ and Cu₂O have their unique Raman-active fundamental modes. D band (1360 cm⁻¹) and G band (1579 cm⁻¹) of RGO appeared in both TiO₂/RGO and TiO₂/RGO/Cu₂O samples, moreover, the I_D/I_G of RGO has been increased significantly compared with pure GO, which also revealed that the GO has been reduced after calcination and illumination [29,30]. According to Raman spectra of TiO₂ samples, the E_g and A_{1g} are the most prominent modes at 447 cm⁻¹ and 607 cm⁻¹ as well as the second-order scattering features at 237 cm⁻¹ [31]. Raman shift at 96 cm⁻¹ and 215 cm⁻¹ of TiO₂/Cu₂O and TiO₂/RGO/Cu₂O samples can be attributed to T_{2u} and Raman scattering features from Cu₂O, respectively, and the appearance of T_{2u} indirectly suggested that the morphology of Cu₂O should belong to NPs and NNs, which agrees with the SEM images [32–34].

X-ray photoelectron spectroscopy (XPS) was further measured to confirm the existence of Cu, C and O elements. However, the XPS spectra of Ti element cannot be observed in Fig. S1, because the TiO₂ has been covered by RGO and Cu₂O. The Cu 2p_{3/2} and Cu 2p_{1/2} spin-orbital photoelectrons of Cu₂O has appeared at 932 eV and 952 eV [35]. A weak peak at around 943 eV can be attributed to Cu (II), the existence of Cu (II) might be due to the presence of CuO [36], but the quantity of CuO is very little, so the XRD patterns cannot detect the CuO in the sample. XPS spectrum of C1s located at 284 eV can

be corresponded to C–C bond, while a very weak peak at 288 eV resulted from C–O and O–C=O bands, so the XPS spectrum further proved that the GO has been reduced to RGO [37].

TEM image of TiO₂/RGO/Cu₂O powder (stripped from photoelectrodes and then ultrasonic dispersed in ethanol for 5 min) was observed in Fig. 5a. The TiO₂ NWs with an average width of 160 nm, Cu₂O NPs and narrow Cu₂O NNs can be evidently observed on the RGO NSs. To further characterize the sample, HR-TEM was carried out. The lattice fringe of 0.246 nm corresponding to the reflections from (1 1 1) plane of Cu₂O has been shown in Fig. 5b [35], confirming that Cu₂O has been successfully introduced on surface of RGO film. The scanning transmission electron microscope (STEM) and energy dispersive X-ray spectroscopy (EDX) elemental mapping were also characterized in order to analyze the distribution of TiO₂, RGO and Cu₂O on FTO substrate. Base on the STEM images (Fig. 6), the morphology of sample stripped from FTO samples was constituted of broken NWs, NPs and NSc, and Cu₂O NPs were quite uniformly coated on the RGO NSs. Combining STEM images and EDX elemental mapping, the large NWs belong to TiO₂, and homodisperse NPs and small NNs can be attributed to Cu₂O, which is consistent with SEM images. Moreover, the RGO NSs could be also easily distinguished from the C–K images. Therefore, the STEM and EDX data accurately proved the existence of heterostructure built from three different components.

Generally, responding ability to solar light is one of most important factors for evaluating photoelectrode performance, since the spectral absorption range would directly influence the number of photogenerated electrons and holes. Therefore, UV–vis absorption spectra of samples were characterized as shown in Fig. 7. The bare TiO₂ photoelectrode exhibited relative narrow band from 200 to 400 nm at UV region, due to its wide bandgap [38]. The slight dark color of RGO partially expands the absorption spectra, but RGO took little contribution to spectra responding ability of photoelectrode, because RGO has no obvious bandgap [39]. According to the absorption spectra of bare Cu₂O, the introduction of Cu₂O has successfully endowed TiO₂ photoelectrode with wide spectral absorption range, and their absorption intensities located at visible light have been enhanced with increasing the quantity of Cu₂O. Therefore,

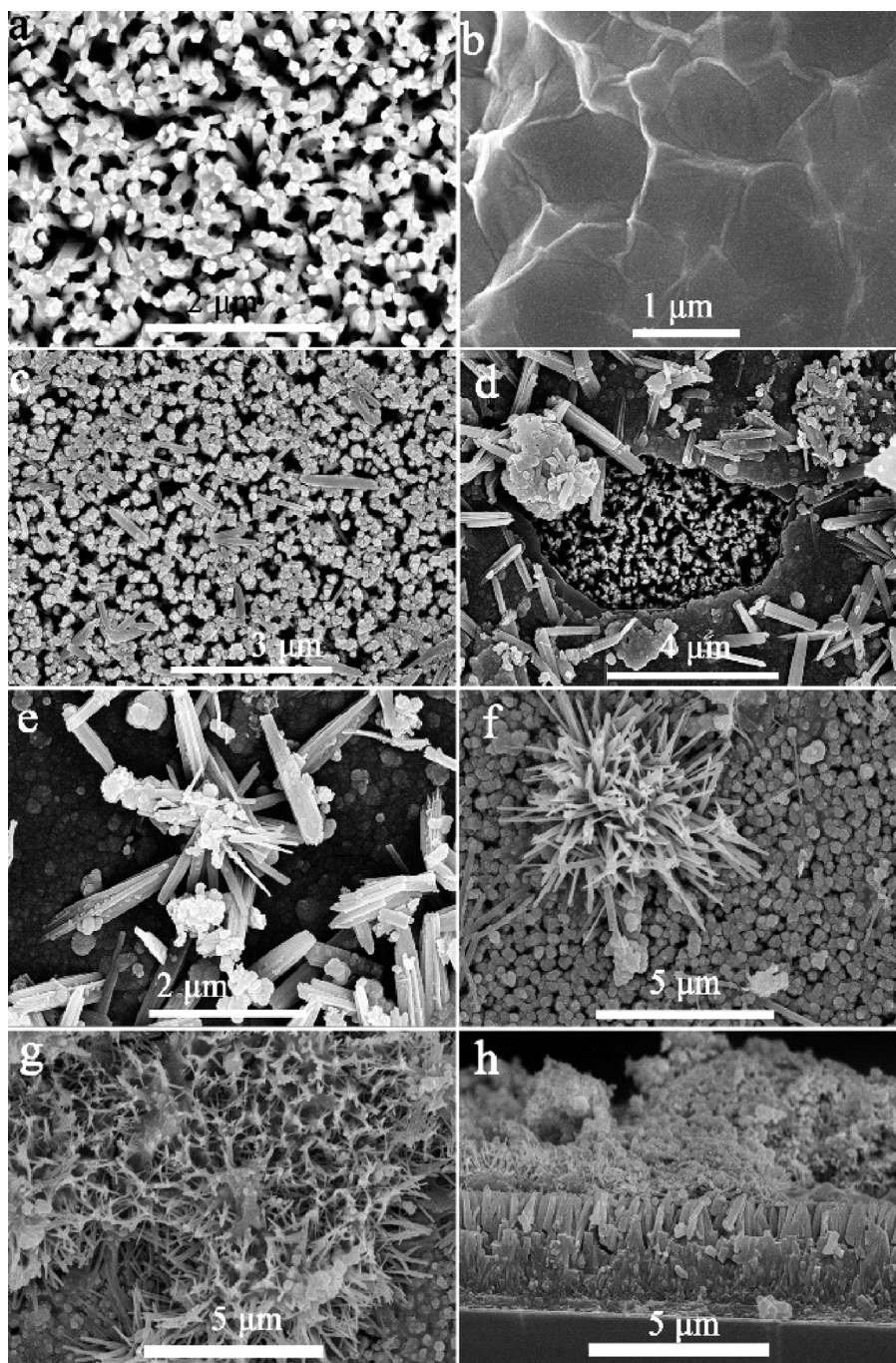


Fig. 2. FE-SEM images. TiO_2 (a), TiO_2/RGO (b), $\text{TiO}_2/\text{Cu}_2\text{O}$ (cycle time = 60) (c), $\text{TiO}_2/\text{RGO}/\text{Cu}_2\text{O}$ (cycle time = 30) (d and e), $\text{TiO}_2/\text{RGO}/\text{Cu}_2\text{O}$ (cycle time = 60) (f), $\text{TiO}_2/\text{RGO}/\text{Cu}_2\text{O}$ (cycle time = 90) (g), Cross-sectional images of $\text{TiO}_2/\text{RGO}/\text{Cu}_2\text{O}$ (cycle time = 60) (h).

fabrication of $\text{TiO}_2/\text{RGO}/\text{Cu}_2\text{O}$ heterostructure can be applied as a valid strategy to solve the limitation of bare TiO_2 photoelectrode.

The linear sweep voltammogram measurements were studied in a three-electrode system. The obtained samples were employed as working electrodes, while Ag/AgCl (soaked in saturated KCl), Pt wire and 0.5 M Na_2SO_4 solution (pH = 7) were utilized as reference electrode, counter electrode and electrolyte, respectively. Fig. 8a presents the photocurrents and darkcurrents of different samples. All the photocurrents showed outstanding performances compared with the darkcurrents, due to the light responding ability of electrodes [40]. However, the photocurrent intensity of bare TiO_2 electrode merely reached to $0.02 \text{ mA}/\text{cm}^2$ at 0.8 V, which could be attributed to the slow transmission of charge and recombination

of electron–hole pairs. The photocurrent intensities of TiO_2/RGO and $\text{TiO}_2/\text{Cu}_2\text{O}$ samples have been obviously improved compared with bare TiO_2 and Cu_2O (Fig. S2) samples. After further modification with both RGO and Cu_2O , the $\text{TiO}_2/\text{RGO}/\text{Cu}_2\text{O}$ photoelectrode exhibited higher photocurrent (more than $0.1 \text{ mA}/\text{cm}^2$ at 0.8 V), which reached almost 5 times than that of bare TiO_2 .

To investigate influence of the amount of Cu_2O on photoelectrochemical performance, linear sweep voltammograms of $\text{TiO}_2/\text{RGO}/\text{Cu}_2\text{O}$ samples with different loading cycle times of Cu_2O have been characterized (Fig. 8b). The results show that all $\text{TiO}_2/\text{RGO}/\text{Cu}_2\text{O}$ samples exhibited better photocurrent than TiO_2/RGO at 0.8 V, due to the effective mode composed of Cu_2O , RGO and TiO_2 . It is worth noting that the photocurrent of

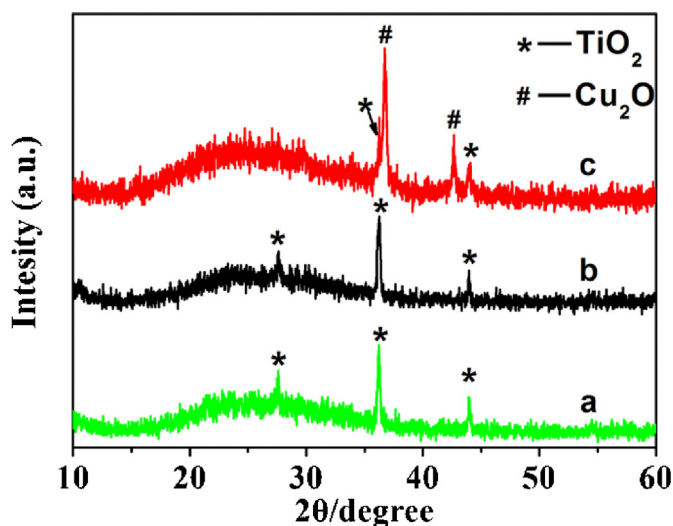


Fig. 3. XRD patterns of TiO_2 , TiO_2/RGO and $\text{TiO}_2/\text{RGO}/\text{Cu}_2\text{O}$.

$\text{TiO}_2/\text{RGO}/\text{Cu}_2\text{O}$ ($\text{Cu}_2\text{O} = 60$ times) is much higher than those of others ($\text{Cu}_2\text{O} = 0, 30, 90$ times), and the alternation of photocurrent intensity might be attributed to the amount and morphology of Cu_2O . Taking account of SEM images, more Cu_2O NSCs were gradually formed on RGO NSs with increasing Cu_2O quantity, and then Cu_2O NSCs generally became integral, of which the unique microstructure would help the light absorption and charge transform due to large surface area of 3D NSC [41,42]. However, excess Cu_2O NSCs contrarily reduced responding area of TiO_2 NWs to UV light, causing the depressed photocurrent intensity when the cycle time was up to 90. Therefore, $\text{TiO}_2/\text{RGO}/\text{Cu}_2\text{O}$ ($\text{Cu}_2\text{O} = 60$ times) as the optimal designed heterostructure photoelectrode showed the best photocurrent intensity among all samples.

The corresponding mechanism of electron transfer has been illustrated in Fig. 9, the p–n heterojunction composed of n-type TiO_2 and p-type Cu_2O has been fabricated in the heterostructure, and the conduction band of Cu_2O is more negative than that of TiO_2 , so the photogenerated electrons can transfer from Cu_2O to TiO_2 . More importantly, the RGO film as electronic exchange medium further enhanced the interface interaction and favored electrons transfer ability between Cu_2O and TiO_2 . Therefore, both $\text{TiO}_2/\text{Cu}_2\text{O}$ heterostructure and advantage of RGO have played an important role in increasing charge separation of electron–hole pairs. On the other hand, the introduction of Cu_2O has also extended the light absorption range of $\text{TiO}_2/\text{RGO}/\text{Cu}_2\text{O}$ sample.

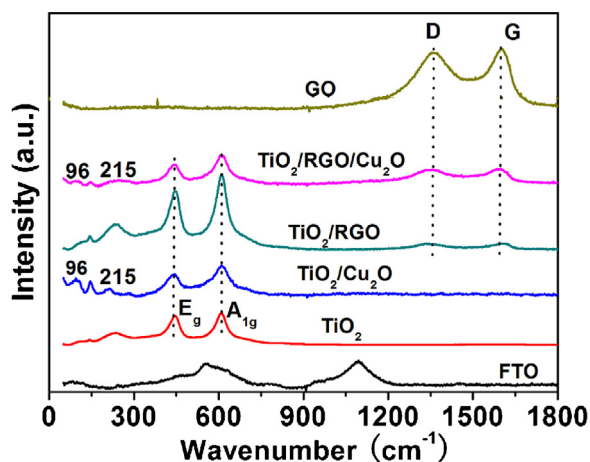


Fig. 4. Raman spectra of FTO, TiO_2 , $\text{TiO}_2/\text{Cu}_2\text{O}$, TiO_2/RGO , $\text{TiO}_2/\text{RGO}/\text{Cu}_2\text{O}$ and GO.

Electrochemical impedance spectroscopy (EIS) measurements (Fig. 10) were carried out covering the frequency range of $0.01 - 10^6$ Hz to investigate the charge transfer process at the semiconductor–electrolyte interface. The EIS data could be fitted with equivalent circuit as the insert image (R_s – solution resistance, R_{ct} – charge transfer resistance, CPE – constant phase angle element and W_d – Warburg element), and the diameter of the semi-circle directly revealed the charge-transfer resistance [43,44]. The R_{ct} values of TiO_2 , TiO_2/RGO , $\text{TiO}_2/\text{Cu}_2\text{O}$ and $\text{TiO}_2/\text{RGO}/\text{Cu}_2\text{O}$ (60) were 1484Ω , 185Ω , 150Ω and 105Ω , respectively. The R_{ct} values of both TiO_2/RGO and $\text{TiO}_2/\text{Cu}_2\text{O}$ were sharply smaller than that of bare TiO_2 , indicating that the excellent conductivity of RGO and p–n junction effect of Cu_2O have significantly accelerated the electron mobility by depressing the recombination of electron–hole pairs [45–47]. $\text{TiO}_2/\text{RGO}/\text{Cu}_2\text{O}$ exhibited the lowest charge-transfer resistance, which further suggested that the ternary heterostructure optimized the photoelectrochemical actives of bare TiO_2 .

Conversion efficiency of light based on heterostructure photoelectrode was studied in-depth. IPCE values of all samples have been carried out under monochromatic light illumination at 0.6 V vs Ag/AgCl (Fig. 11), which were calculated according to following equation:

$$\text{IPCE} = 1240 \times \frac{I_{ph}}{\lambda \times J_{light}}$$

I_{ph} is photocurrent density (mA/cm^2), λ is wavelength of incident light, and J_{light} is incident light power density (mW/cm^2) on electrodes at each wavelength [48,49]. Under 0.6 V vs Ag/AgCl, the maximum IPCE value of $\text{TiO}_2/\text{RGO}/\text{Cu}_2\text{O}$ was measured to be about 55% under the incident light at 370–400 nm, which is much higher than bare TiO_2 (19% at 330 nm), TiO_2/RGO (29% at 350 nm) and $\text{TiO}_2/\text{Cu}_2\text{O}$ (33% at 370 nm). $\text{TiO}_2/\text{RGO}/\text{Cu}_2\text{O}$ (60) shows the best capability among all samples, and this result is consistent with the photocurrent measurements. More attention should be paid that IPCE value of $\text{TiO}_2/\text{RGO}/\text{Cu}_2\text{O}$ heterostructure appeared obvious peak in the visible region from 425 to 450 nm, which further revealed the important role of Cu_2O in heterostructure [50,51]. On the basis of the I – V curves and IPCE values, fabrication of $\text{TiO}_2/\text{RGO}/\text{Cu}_2\text{O}$ heterostructure could significantly improve the photoelectric conversion efficiency of photoelectrode.

The hydrogen production equipment was held at 0.6 V vs calomel electrode under xenon lamp illumination for hydrogen generation, and the schematic diagram of corresponding equipment was shown in Fig. 12. Hydrogen production rate was measured and calculated through gas chromatography [52,53]. A three-electrode system was also utilized, in which working electrode is heterostructure in 20% methanol aqueous solution, while the counter electrode is Pt plate in deionized water for hydrogen evolution. The $\text{TiO}_2/\text{RGO}/\text{Cu}_2\text{O}$ electrodes in this system played an important role in the accumulation of holes, and the holes was mainly used to oxidize methanol to formaldehyde, which significantly improves the separation of photogenerated electrons and holes. And the electrons would transfer to Pt electrode for hydrogen production.

The hydrogen production rates (Fig. 13a) of TiO_2 and $\text{TiO}_2/\text{RGO}/\text{Cu}_2\text{O}$ (60) photoelectrodes are average $211.8 \mu\text{mol}/\text{h m}^2$ and $631.6 \mu\text{mol}/\text{h m}^2$, respectively. The above-mentioned result indicates that the introduction of RGO and Cu_2O can not only inhibit the recombination of electron–hole pairs, but also enhance the efficiency of charges transfer, which is suitable for hydrogen production by photoelectrochemical water splitting. Furthermore, the stability of $\text{TiO}_2/\text{RGO}/\text{Cu}_2\text{O}$ photoelectrode was valued by the I – t curve for water splitting as shown in Fig. 13b. The photocurrent intensity kept stable on the whole, after 10 h for water splitting. However, a strange phenomenon of increased current density has

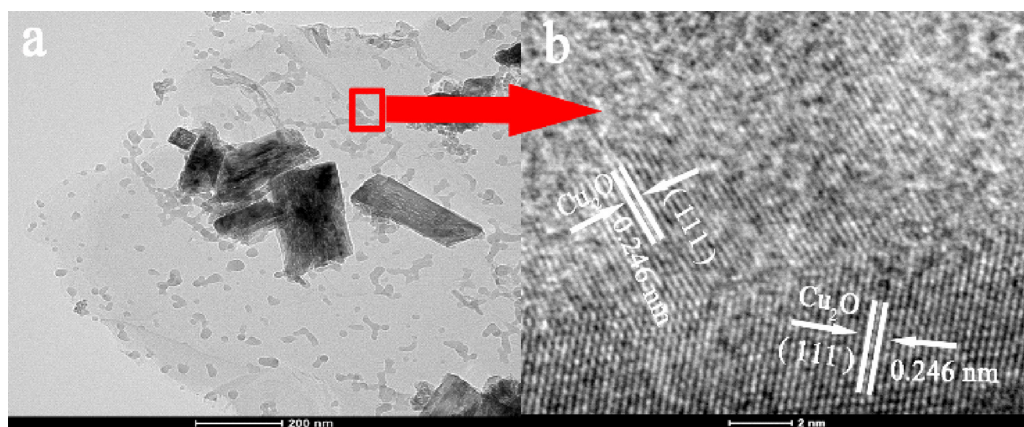


Fig. 5. TEM (a) and HR-TEM (b) images of TiO₂/RGO/Cu₂O samples.

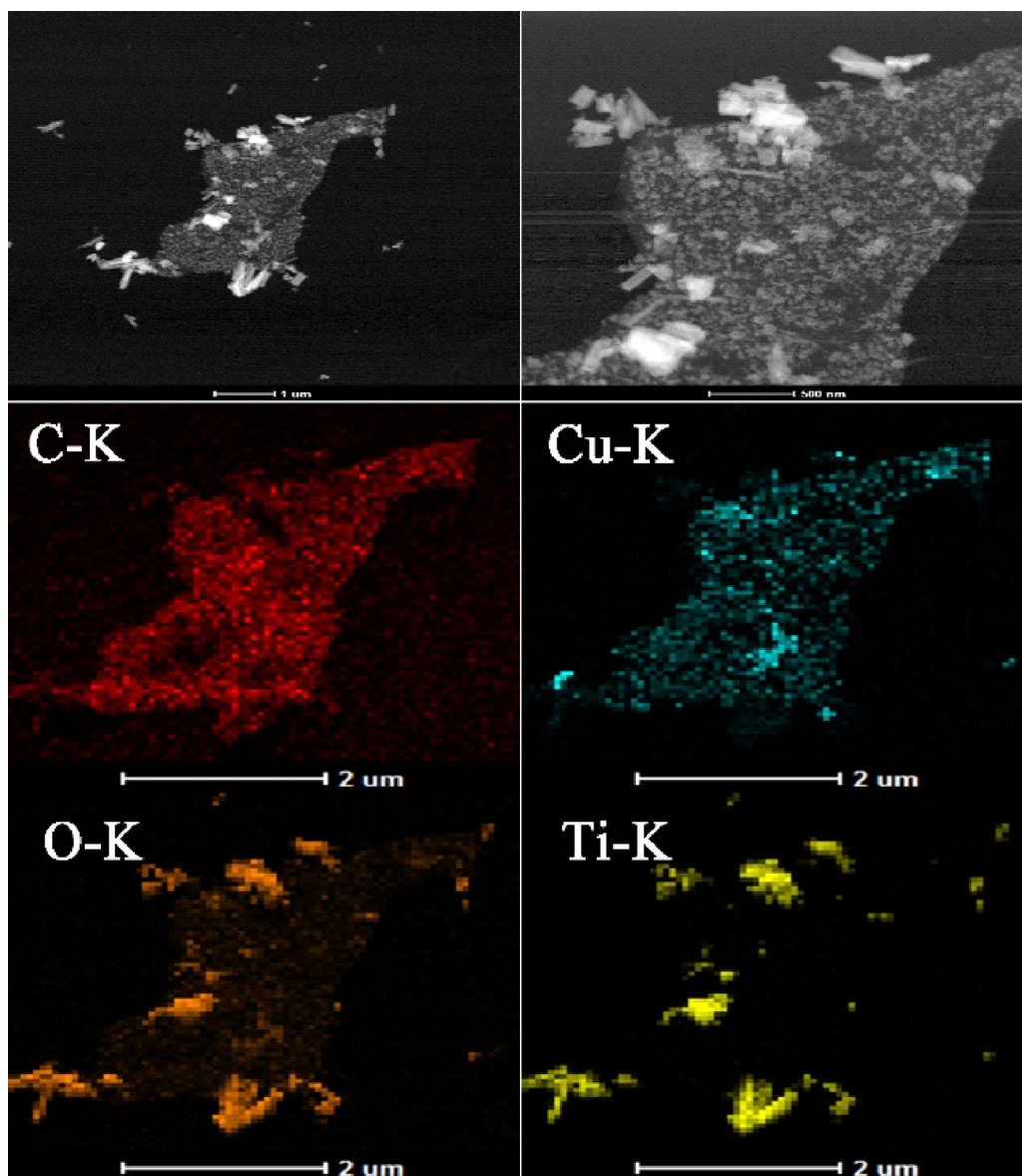


Fig. 6. STEM images and corresponding EDX elemental mapping of C, Cu, O and Ti of TiO₂/RGO/Cu₂O.

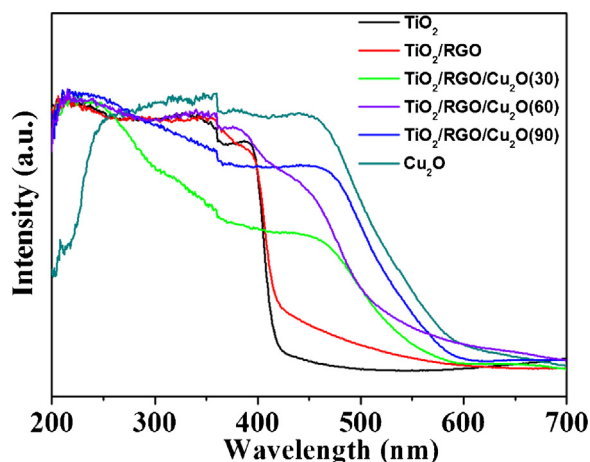


Fig. 7. UV-vis absorption spectra.

appeared, when $\text{TiO}_2/\text{RGO}/\text{Cu}_2\text{O}$ (60) in the hydrogen production system was irradiated for 4 h. In order to explain the problem, SEM image of $\text{TiO}_2/\text{RGO}/\text{Cu}_2\text{O}$ (60), after water splitting under illumination for 5 h, has been measured (Fig. S3). Due to the SEM image, this increased current density may be attributed to the morphology change of Cu_2O , and the similar phenomenon has also been previously reported [54]. Cu_2O with low valence Cu(I) ions tended to be oxidized as Cu(II) by photogenerated holes, but the methanol as sacrificial agent in the hydrogen production system can effectively trap the holes to depress the oxidation of Cu_2O , because the standard

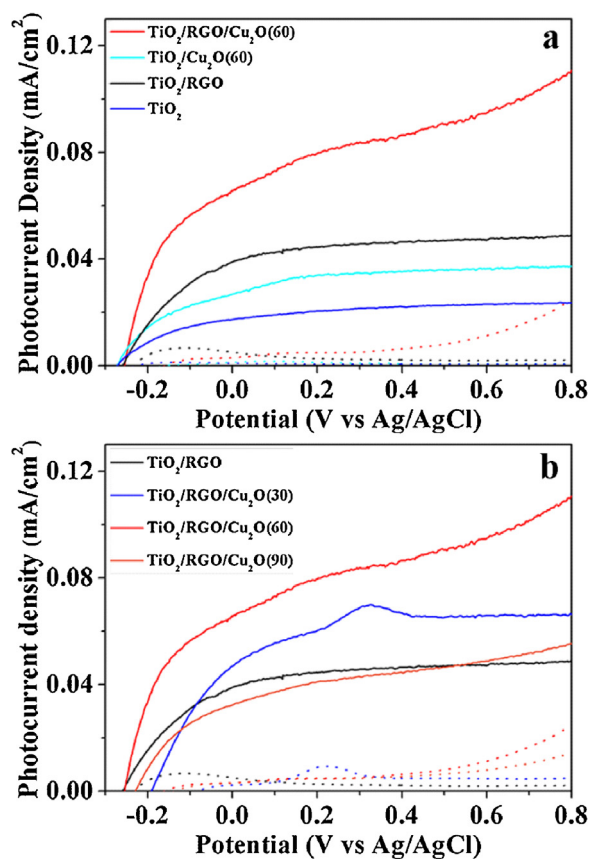


Fig. 8. (a) I - V characteristic curves of TiO_2 , TiO_2/RGO , $\text{TiO}_2/\text{Cu}_2\text{O}$ and $\text{TiO}_2/\text{RGO}/\text{Cu}_2\text{O}$ samples. Photocurrent and dark current were indicated by solid lines and dash lines, respectively. (b) I - V characteristic curves of $\text{TiO}_2/\text{RGO}/\text{Cu}_2\text{O}$ samples with different cycle times.

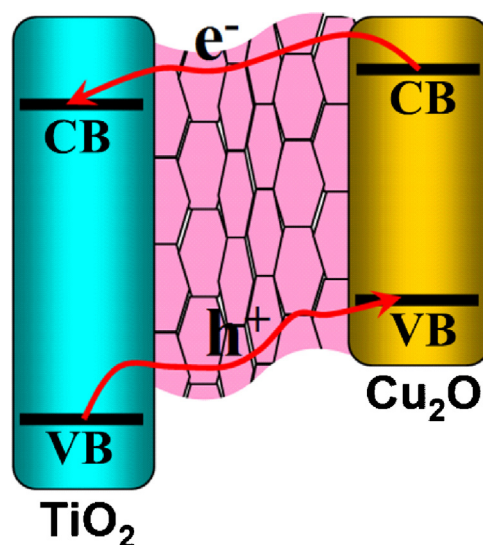


Fig. 9. Schematic illustration of electron transfer mechanism.

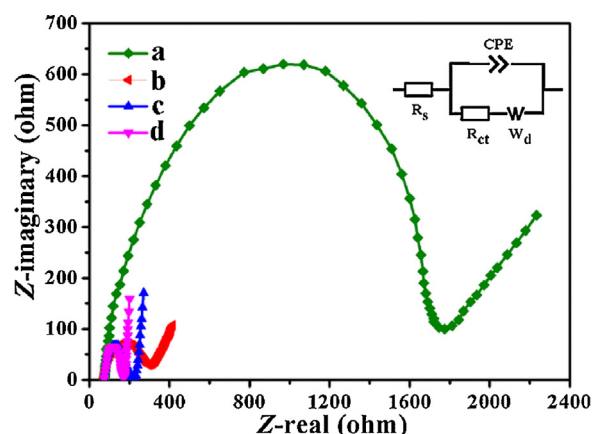


Fig. 10. Nyquist plots of TiO_2 (a), TiO_2/RGO (b), $\text{TiO}_2/\text{Cu}_2\text{O}$ (c), $\text{TiO}_2/\text{RGO}/\text{Cu}_2\text{O}$ (60) (d) measured at 0.2 V vs Ag/AgCl ; the insert image is the equivalent circuit model for photoanodes.

oxidation potential of methanol ($E^\theta_{\text{HCHO(aq)}/\text{CH}_3\text{OH(aq)}} = 0.13 \text{ V}$) is lower than that of Cu_2O ($E^\theta_{\text{Cu(II)}/\text{Cu(I)}} = 0.16 \text{ V}$) [55]. As a result, $\text{TiO}_2/\text{RGO}/\text{Cu}_2\text{O}$ heterostructure showed a great potential for application in photoelectrochemical hydrogen production.

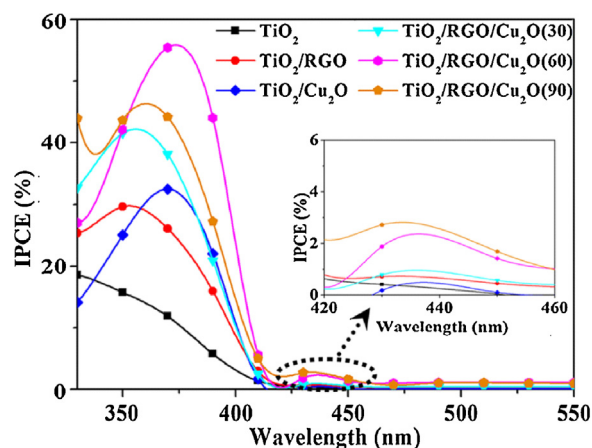


Fig. 11. IPCE values recorded for TiO_2 , TiO_2/RGO , $\text{TiO}_2/\text{Cu}_2\text{O}$, $\text{TiO}_2/\text{RGO}/\text{Cu}_2\text{O}$ with 30, 60 and 90 cycle times.

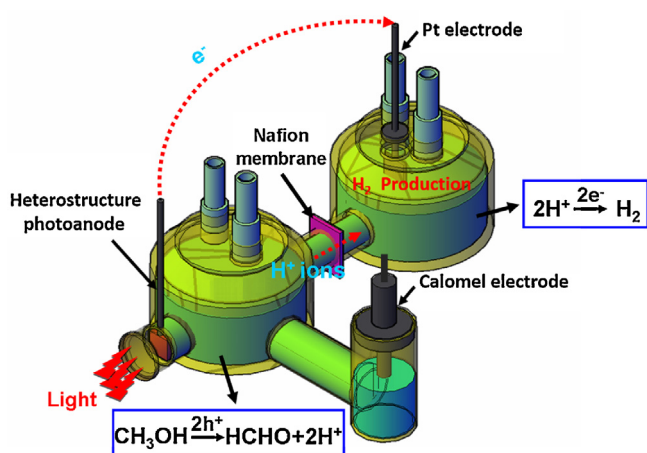


Fig. 12. Schematic diagram of equipment for photoelectrochemical hydrogen production.

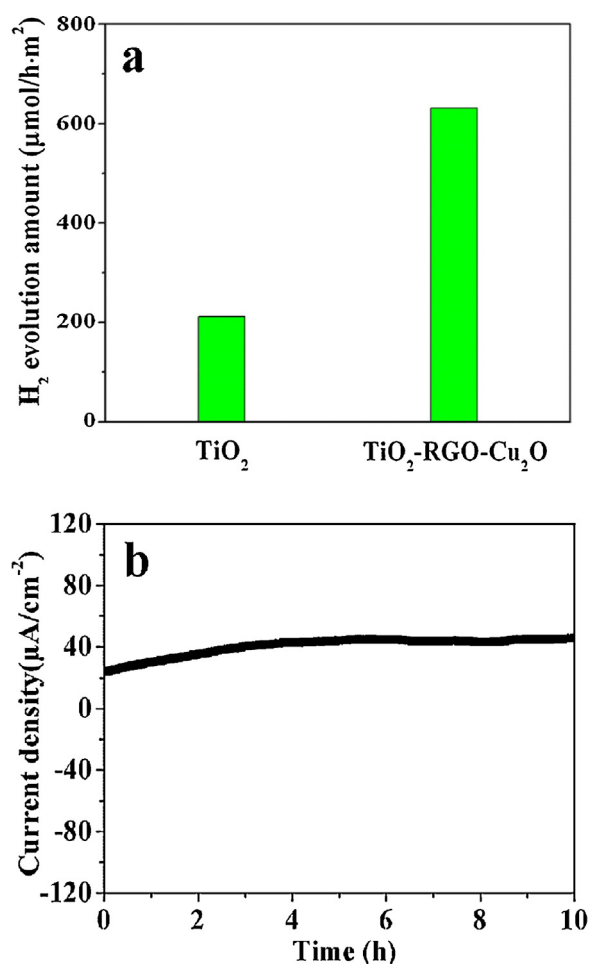


Fig. 13. Hydrogen production rates of TiO₂ and TiO₂/RGO/Cu₂O (60) samples at 0.6 V vs Calomel electrode under xenon lamp illumination (47 mW cm²) (a) and the *I*-*t* curve for water splitting (b).

4. Conclusions

TiO₂/RGO/Cu₂O heterostructure constituted by TiO₂ NWs, RGO NSs and Cu₂O have been successfully synthesized and characterized. Raman, UV-vis absorption, HR-TEM and STEM confirmed the successful preparation of TiO₂/RGO/Cu₂O heterostructure. TiO₂/RGO/Cu₂O (60) exhibited significantly enhanced

photoelectrochemical performance, including high photocurrent density, IPCE value and hydrogen production, due to the synergistic effect of TiO₂, RGO and Cu₂O. EIS data also proved that TiO₂/RGO/Cu₂O heterostructure took a nature of lowest charge-transfer resistance. Hydrogen production rate and stability further revealed the excellent performance of TiO₂/RGO/Cu₂O heterostructure, so this work offered an alternative strategy to design and fabricate multivariate heterostructure for photoelectrochemical water splitting.

Acknowledgements

The authors are grateful for National Natural Science Foundation of China (21401082, and 21201085), Natural science foundation of Jiangsu Province (BK2012294 and BK20141305), Special Financial Grant from the China Postdoctoral Science Foundation (2014T70473), Open Project of State Key Laboratory of Rare Earth Resource Utilizations (RERU2015004), Youth Backbone Teacher Training Engineering of Jiangsu University and Chinese-German Cooperation Research Project (GZ1091).

Appendix A. Supplementary data

Supplementary data associated with this article can be found, in the online version, at <http://dx.doi.org/10.1016/j.apcatb.2015.07.032>

References

- [1] F.E. Osterloh, B.A. Parkinson, *MRS Bull.* 36 (2011) 17–22.
- [2] R. Liu, Z. Zheng, J. Spurgeon, B.S. Brunschwig, X.G. Yang, *Energy Environ. Sci.* 7 (2014) 2504–2517.
- [3] C. Zhang, W.Q. Fan, H.Y. Bai, X.Q. Yu, C. Chen, R.X. Zhang, W.D. Shi, *ChemElectroChem* 1 (2014) 2089–2097.
- [4] W.Q. Fan, H.Y. Bai, W.D. Shi, *CrystEngComm* 16 (2014) 3059–3067.
- [5] J.H. Yang, K. Walczak, E. Anzenberg, F.M. Toma, G.B. Yuan, J. Beeman, A. Schwartzberg, Y.J. Lin, M. Hettick, A. Javey, J.W. Ager, J. Yano, H. Frei, L.D. Sharp, *J. Am. Chem. Soc.* 136 (2014) 6191–6194.
- [6] A. Fujishima, K. Honda, *Nature* 238 (1972) 37–38.
- [7] B. Liu, E.S. Aydil, *J. Am. Chem. Soc.* 131 (2009) 3985–3990.
- [8] W.K. Ho, J.C. Yu, J. Lin, J.G. Yu, P.S. Li, *Langmuir* 20 (2004) 5865–5869.
- [9] Z. Chen, A.J. Forman, T.F. Jaramillo, *J. Phys. Chem. C* 117 (2013) 9713–9722.
- [10] T.G. Kim, H.B. Oh, H. Ryu, W.J. Lee, *J. Alloys Compd.* 612 (2014) 74–79.
- [11] J.Y. Tsai, S.J. Chang, T.J. Hsueh, H.T. Hsueh, W.Y. Weng, C.L. Hsu, B.T. Dai, *Nanoscale Res. Lett.* 6 (2011) 575.
- [12] L.X. Yang, S.L. Luo, Y. Li, Y. Xiao, Q. Kang, Q.Y. Cai, *Environ. Sci. Technol.* 44 (2010) 7641–7646.
- [13] P.D. Jongh, D. Vanmaekelbergh, J.J. Kelly, *Chem. Commun.* (1999) 1069–1070.
- [14] L.M. Liu, W.Y. Yang, W.Z. Sun, Q. Li, J.K. Shang, *ACS Appl. Mater. Interfaces* 7 (2015) 1465–1476.
- [15] Z. Kang, X.Q. Yan, Y.F. Wang, Z.M. Bai, Y.C. Liu, Z. Zhang, P. Lin, X.H. Zhang, H.G. Yuan, X.J. Zhang, *Y. Zhang, Sci. Rep.* 5 (2015) 7882.
- [16] S. Guo, G.K. Zhang, Y.D. Guo, J.C. Yu, *Carbon* 60 (2013) 437–444.
- [17] S.J. Hu, B. Chi, J. Pu, L. Jian, *RSC Adv.* 4 (2014) 60437–60444.
- [18] X.F. Yang, J.L. Qin, Y. Jiang, K.M. Chen, X.H. Yan, D. Zhang, R. Li, H. Tang, *Appl. Catal. B: Environ.* 166–167 (2015) 231–240.
- [19] X.F. Yang, J.L. Qin, Y. Jiang, R. Li, Y. Li, H. Tang, *RSC Adv.* 4 (2014) 18627–18636.
- [20] S.D. Sarma, S.Q. Adam, E.H. Hwang, E. Rossi, *Rev. Mod. Phys.* 83 (2011) 407–470.
- [21] D.A. Dikin, S. Stankovich, E.J. Zimney, R.D. Piner, G.H.B. Dommett, G. Evmenenko, S.T. Nguyen, R.S. Ruoff, *Nature* 448 (2007) 457–460.
- [22] S.Y. Toh, K.S. Loh, S.K. Kamarudin, W.R.W. Daud, *Chem. Eng. J.* 251 (2014) 422–434.
- [23] I.S. Cho, Z. Chen, A.J. Forman, D.R. Kim, P.M. Rao, T.F. Jaramillo, X.L. Zheng, *Nano Lett.* 11 (2011) 4978–4984.
- [24] W.Q. Fan, X.Q. Yu, S.Y. Song, H.Y. Bai, C. Zhang, D. Yan, C.B. Liu, W. Qian, W.D. Shi, *CrystEngComm* 16 (2014) 820–825.
- [25] W. Hummers, R. Offeman, *J. Am. Chem. Soc.* 80 (1958), 1339–1339.
- [26] A.G. Tamirat, W.N. Su, A.A. Dubale, C.J. Pan, H.M. Chen, D.W. Ayele, J.F. Lee, B.J. Hwang, *J. Power Sources* 287 (2015) 119–128.
- [27] Y. Hou, F. Zuo, A. Dagg, P. Feng, *Nano Lett.* 12 (2012) 6464–6473.
- [28] Y.H. Ng, A. Iwase, A. Kudo, R. Amal, *J. Phys. Chem. Lett.* 1 (2010) 2607–2612.
- [29] P. Cui, J. Lee, E. Hwang, H. Lee, *Chem. Commun.* 47 (2011) 12370–12372.
- [30] H. Guo, X. Wang, Q. Qian, F. Wang, X. Xia, *ACS Nano* 3 (2009) 2653–2659.
- [31] X.L. Yin, Y.L. Li, F. Ke, C.F. Lin, H.B. Zhao, L. Gan, Z.T. Luo, R.G. Zhao, T.F. Heinz, Z.H. Hu, *Nano Res.* 11 (2014) 1613–1622.

- [32] F.D. Hardcastle, J. Ark. Acad. Sci. 65 (2011) 43–48.
- [33] G. Prabhakaran, R. Murugan, Adv. Mater. Res. 938 (2014) 114–117.
- [34] T. Ohsaka, F. Lzumi, Y. Fujiki, J. Raman Spectrosc. 7 (1978) 321–324.
- [35] M.Y. Wang, L. Sun, Z.Q. Lin, J.H. Cai, K.P. Xie, C.J. Lin, Energy Environ. Sci. 6 (2013) 1211–1220.
- [36] M.A. Mahmoud, W. Qian, M.A. El-Sayed, Nano Lett. 11 (2011) 3285–3289.
- [37] M.H. Cao, P.F. Wang, Y.H. Ao, C. Wang, J. Hou, J. Qian, Chem. Eng. J. 264 (2015) 113–124.
- [38] Z.B. Jiao, T. Chen, J.Y. Xiong, T. Wang, G.X. Lu, J.H. Ye, Y.P. Bi, Sci. Rep. 3 (2013) 2720.
- [39] X.F. Zhang, B.Y. Zhang, D.K. Huang, H.L. Yuan, M.K. Wang, Y. Shen, Carbon 80 (2014) 591–598.
- [40] J.G. Hou, Z. Wang, C. Yang, H.J. Cheng, S.Q. Jiao, H.M. Zhu, Energy Environ. Sci. 6 (2013) 3322–3330.
- [41] Q. Peng, B. Kalanyan, P.G. Hoertz, A. Miller, D.H. Kim, K. Hanson, L. Alibabaei, J. Liu, T.J. Meyer, G.N. Parsons, J.T. Glass, Nano Lett. 13 (2013) 1481–1488.
- [42] Y.J. Jang, J.-W. Jang, S.H. Choi, J.Y. Kim, J.H. Kim, D.H. Youn, W.Y. Kim, S. Hana, J.S. Lee, Nanoscale 7 (2015) 7624–7631.
- [43] B. Klahr, S. Gimenez, F. Fabregat-Santiago, J. Bisquert, T.W. Hamann, J. Am. Chem. Soc. 134 (2012) 16693–16700.
- [44] L. Wang, F. Dionigi, N.T. Nguyen, R. Kirchgeorg, M. Gliech, S. Grigorescu, P. Strasser, P. Schmuki, Chem. Mater. 27 (2015) 2360–2366.
- [45] B.M. Almeida, M.A. Melo Jr., J. Bettini, J.E. Benedetti, A.F. Nogueira, Appl. Surf. Sci. 324 (2015) 419–431.
- [46] A. Wang, X.S. Li, Y.B. Zhao, W. Wu, J.F. Chen, H. Meng, Powder Technol. 261 (2014) 42–48.
- [47] X.Q. An, K.F. Li, J.W. Tang, ChemSusChem 7 (2014) 1086–1093.
- [48] J.M. Macak, H.K. Tsuchiya, A. Ghicov, P. Schmuki, Electrochem. Commun. 7 (2005) 1133–1137.
- [49] Y.J. Hwang, C. Hahn, B. Liu, P.D. Yang, ACS Nano 6 (2012) 5060–5069.
- [50] S. Ho-Kimura, S.J.A. Moniz, J.W. Tang, I.P. Parkin, ACS Sustain. Chem. Eng. 3 (2015) 710–717.
- [51] C.M. McShane, K.-S. Choi, J. Am. Chem. Soc. 131 (2009) 2561–2569.
- [52] J.G. Hou, C. Yang, H.J. Cheng, S.Q. Jiao, O. Takeda, H.M. Zhu, Energy Environ. Sci. 7 (2014) 3758–3768.
- [53] R. Abe, M. Higashi, J. Am. Chem. Soc. 132 (2010) 11828–11829.
- [54] Q. Yu, X.G. Meng, T. Wang, P. Li, L.Q. Liu, K. Chang, G.G. Liu, J.H. Ye, Chem. Commun. 51 (2015) 3630–3633.
- [55] A.J. Bard, R. Parsons, J. Jordan, Standard Potentials in Aqueous Solution, Marcel Dekker Inc. Press, New York, USA, 1985.